Electronic Supplementary Information

Experimental section

Materials: All chemical reagents were purchased from commercial suppliers and were used as received without further purification. Carbon cloth was bought from was provided by Hongshan District, Wuhan Instrument Surgical Instruments business. Water used throughout all experiments was purified by a Millipore ultrapure water system.

Preparation of $NiFe_2O_4$/CC: In a typical process, 0.475 g $NiCl_2{\cdot}6H_2O$, 1.08 g $FeCl_3{\cdot}6H_2O$, 0.37 g NH_4F, and 0.60 g urea were dissolved in 40 mL deionized water. Then the solution was poured into a 50 mL Teflon-lined autoclave with a piece of carbon cloth (2 cm × 3 cm). The autoclave was sealed and heated at 140 °C for 10 h. To prepare $NiFe_2O_4$/CC, the resulting precursor was taken out and annealed at 400 °C under Ar atmosphere for 2 h. The mass loading of $NiFe_2O_4$ nanosheets on CC is 1.8 mg/cm^2.

Preparation of Fe_3O_4/CC: Fe_3O_4 precursor on CC was synthesized by a similar procedure as mentioned above, but without adding $NiCl_2{\cdot}6H_2O$. Then the precursor was annealed at 400 °C under H_2/Ar atmosphere for 2 h to get Fe_3O_4/CC. The mass loading of Fe_3O_4 nanorods on CC is 1.7 mg/cm^2.

Characterizations: SEM measurements were carried out on a Gemini Sigma 300/VP microscope. TEM images were collected on a HITACHI H-8100 electron microscopy. XRD data were acquired by a LabX XRD-6100 X-ray diffraction instrument. XPS

spectra were recorded on an ESCALABMK II X-ray photoelectron spectrometer. UV-Vis absorbance spectra were obtained on a SHIMADZU UV-2700 spectrophotometer. Gas chromatography analysis was performed on a Shimadzu GC-2014C with Ar as carrier gas. ^{1}H NMR spectra were collected on Varian VNMRS 600 MHz (the USA) with water suppression.

Electrochemical measurements: All electrochemical measurements were performed in an H-shaped electrochemical cell with a CHI 760E electrochemical workstation (Shanghai, Chenhua). The electrolyte was Ar-saturated of 0.1 M PBS with 0.1 M $NaNO_3$, using $NiFe_2O_4$/CC as the working electrode, a graphite plate as the counter electrode, and a saturated Ag/AgCl as the reference electrode. All potentials reported in this work were converted to RHE scale and current density was normalized to geometric area of electrode (0.25 cm^2).

Determination of NH_3: The amount of NH_3 in the electrolyte was quantitatively determined by colorimetry using the indophenol blue method. Concretely, 2.0 mL of sample solution was added to a 7 mL of centrifuge tube, to which 2.0 mL of chromogenic reagent (0.1 M sodium hydroxide + 5.0 wt% salicylic acid + 5.0 wt% sodium citrate), 1.0 mL of oxidizing reagent (0.05 M NaClO), and 0.2 mL of catalysing reagent (1.0 wt% sodium nitroferricyanide) were successively added. After 2 h of dark incubation, the absorbance at 655 nm was collected using UV-vis spectrophotometer. The concentration-absorption spectra were calibrated using standard NH_4Cl solution with different concentration (Fig. S1).

Determination of NO_2^-: The amount of NO_2^- in the electrolyte was quantitatively determined by Griess method. In detail, 1.0 mL of sample solution, 1.0 mL of deionized water, and 2.0 mL of Griess reagent (0.2 wt% N-(1-naphthyl)ethyldiamine dihydrochloride + 2.0 wt% sulfonamide + 5.5 wt% H_3PO_4) were successively added to a 7 mL of centrifuge tube. After 15 min of dark incubation, the absorbance at 540 nm was collected using UV-vis spectrophotometer. The concentration-absorption spectra were calibrated using standard $NaNO_2$ solution with different concentration (Fig. S2).

Determination of N_2H_4: The amount of N_2H_4 in the electrolyte was quantitatively determined by Watt and Chrisp method. Firstly, 1.0 mL of sample solution was mixed with 1.0 mL of chromogenic reagent (5.99 g p-dimethylaminobenzaldehyde + 30 mL concentrated HCl + 300 mL ethanol). Then, after incubating in the dark for 15 min, the absorbance at 455 nm was collected using UV-vis spectrophotometer. The concentration-absorption spectra were calibrated using standard N_2H_4 solution with different concentration (Fig. S3).

NO_3^- isotopic labelling experiment: The generated $^{15}NH_4^+$ and $^{14}NH_4^+$ were verified by isotope-labelled tracer experiments using 0.1 M $Na^{15}NO_3$ and $Na^{14}NO_3$ as nitrogen sources, respectively. After 1 h of chronoamperometry test at –1.0 V vs. RHE, the pH of the post-electrolysis electrolyte was adjusted to 2 with 0.5 M HCl. Then, the electrolyte (500 μL) was mixed with D_2O (50 μL) for further ^1H NMR detection.

Determination of NH_3 yield and FE:

$$\mathrm{FE} = \frac{nCVF}{MQ}$$

$$\mathrm{NH_3\ yield} = \frac{CV}{17tA}$$

Where n is the number of electrons transferred during eNO_3RR, C is the concentration of products, V is the volume of cathodic electrolyte, F is the Faraday constant, M is the molar mass of products, Q is the total quantity of applied electricity, t is the electrolysis time, and A is the geometric area of working electrode.

Computational details: First-principles calculations with spin-polarized were performed based on density functional theory implemented in the VASP package,[1] and the interaction between valence electrons and ionic core were expanded using the projector augmented wave (PAW)[2] approach with a cutoff of 450 eV. Perdew-Burke-Ernzerhof functional (PBE) with semi-empirical corrections of DFT-D3 was adopted to describe exchange-correlation functional effect[3] based on general gradient approximation (GGA). $NiFe_2O_4$ (100) surface with two terminations were modeled, the thickness of the vacuum region is >15 Å to avoid the spurious interaction. Hubbard U model was implemented with an effective U = 4.5 eV and 4 eV for Fe 3d and Ni 3d orbitals, respectively.[4,5] The Brillouin zone was sampled by 3 × 3 × 1 special k-points using the Monkhorst Pack scheme for structural configuration optimizations.[6] The force convergence thresholds are 0.02 eV/Å and the total energy less than 1E-5 eV, respectively. The theoretical calculation results were processing and analyzed by VASPKIT software.[7]

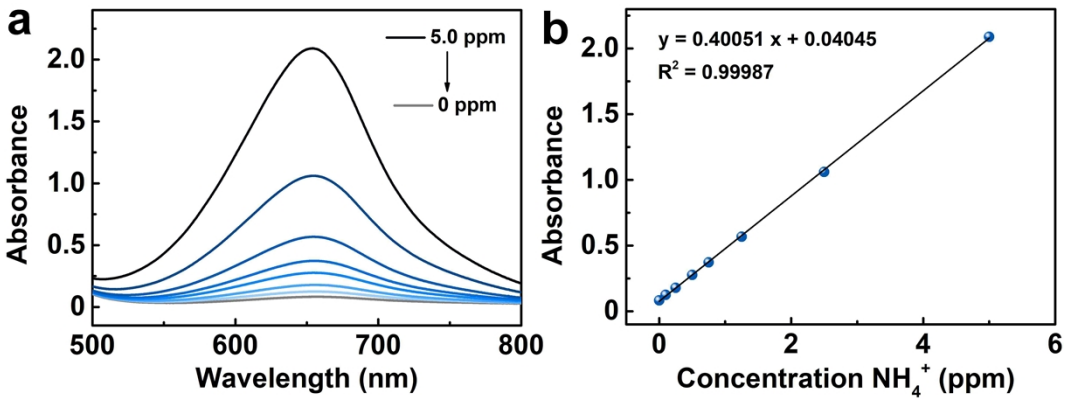

Fig. S1. Plotting of standard curve of NH_4^+ in 0.1 M PBS solution.

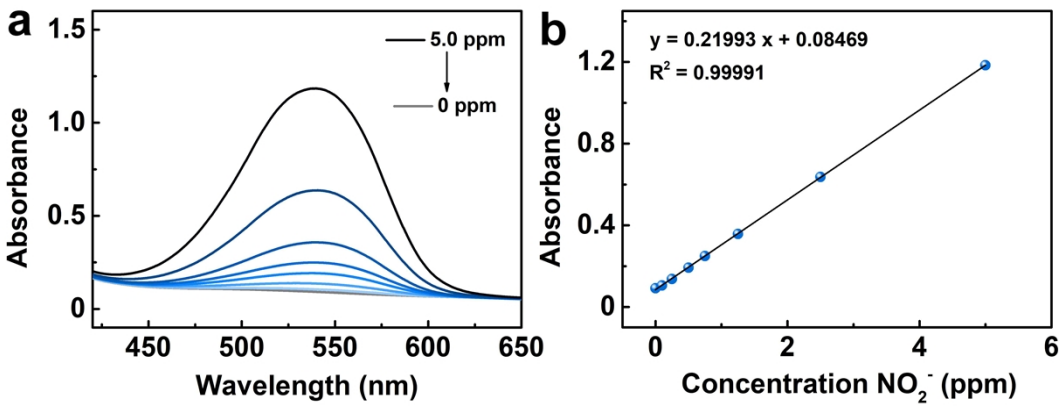

Fig. S2. Plotting of standard curve of NO_2^- in 0.1 M PBS solution.

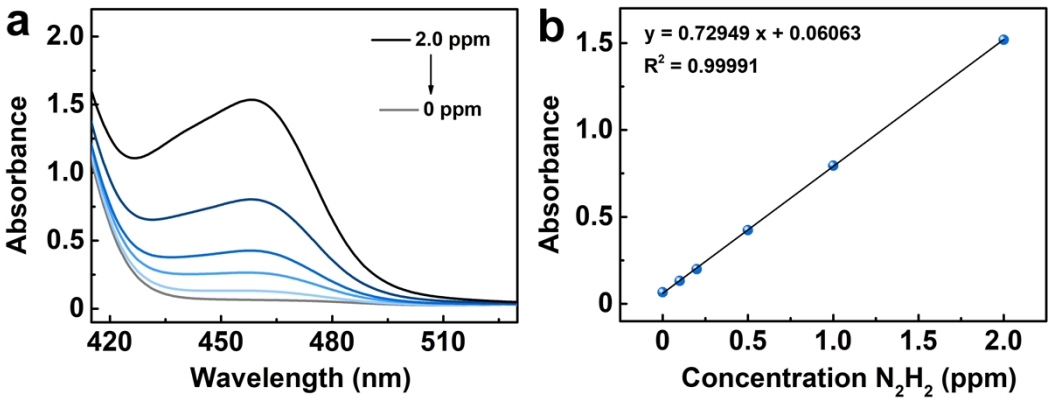

Fig. S3. Plotting of standard curve of N_2H_4 in 0.1 M PBS solution.

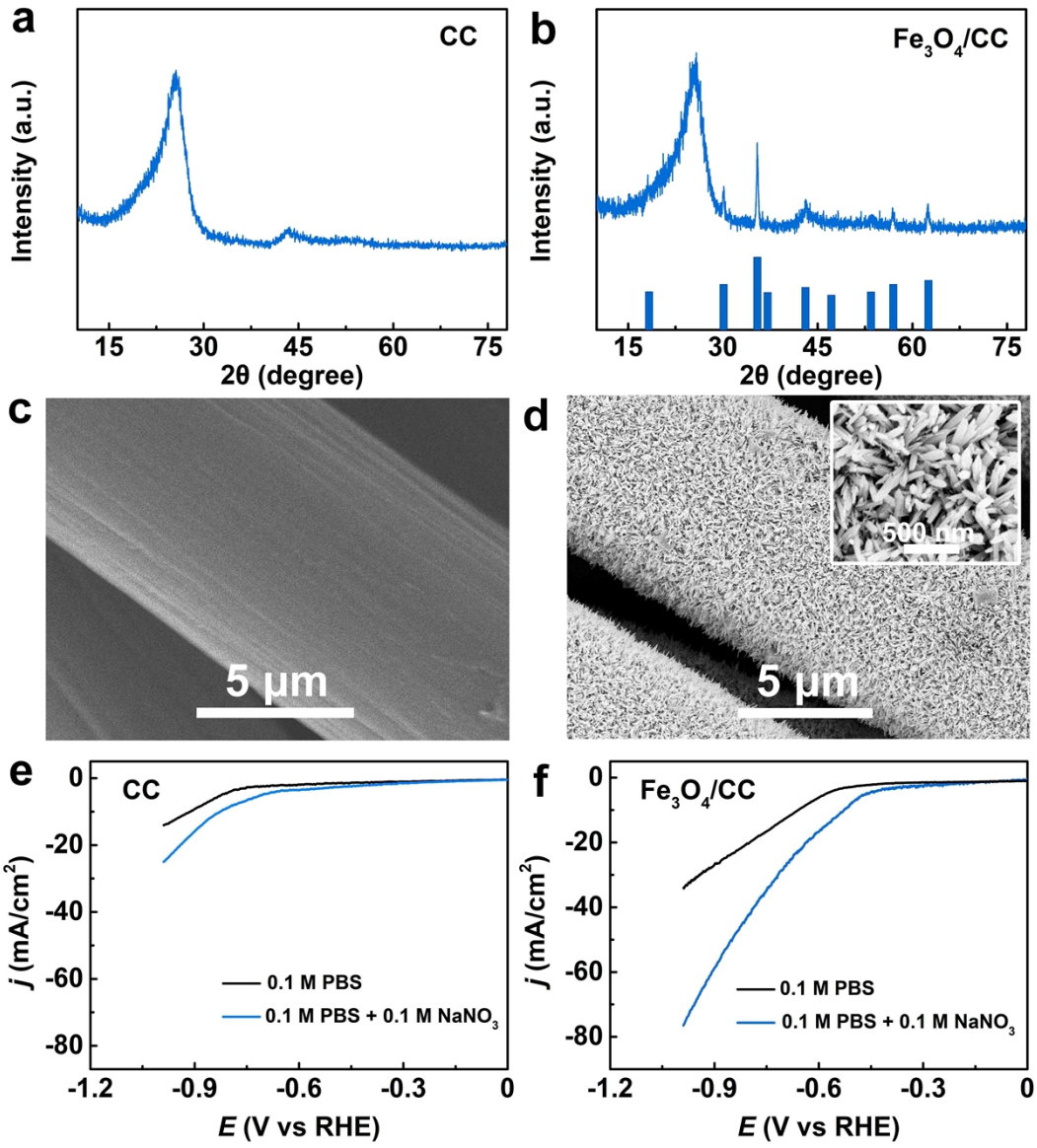

Fig. S4. XRD patterns of (a) CC and (b) Fe_3O_4/CC. SEM images of (c) CC and (d) Fe_3O_4/CC. LSV curves of (e) CC and (f) Fe_3O_4/CC in Ar-saturated 0.1 M PBS with/without additional 0.1 M $NaNO_3$.

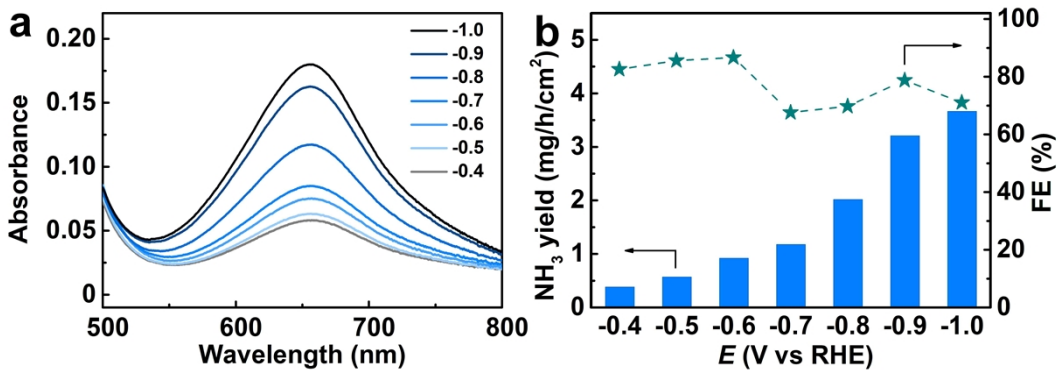

Fig. S5. (a) UV-Vis spectra of generated NH_3 for Fe_3O_4/CC at each given potential. (b) Corresponding NH_3 yields and FEs.

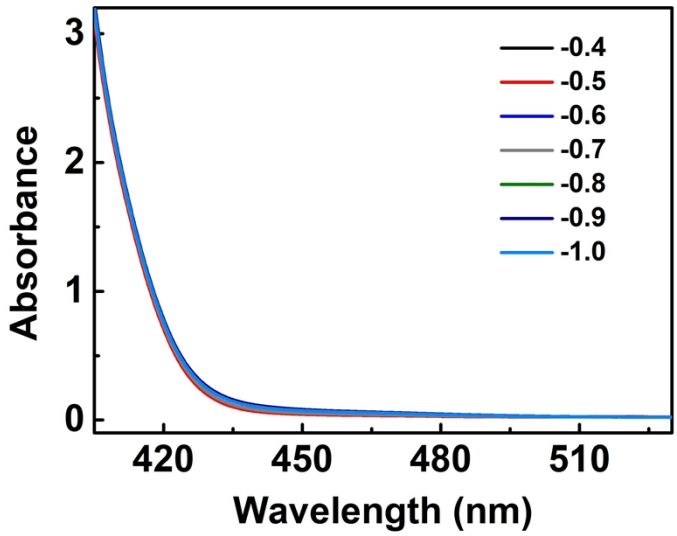

Fig. S6. UV-Vis spectra of generated N_2H_4 for $NiFe_2O_4$/CC at each given potential.

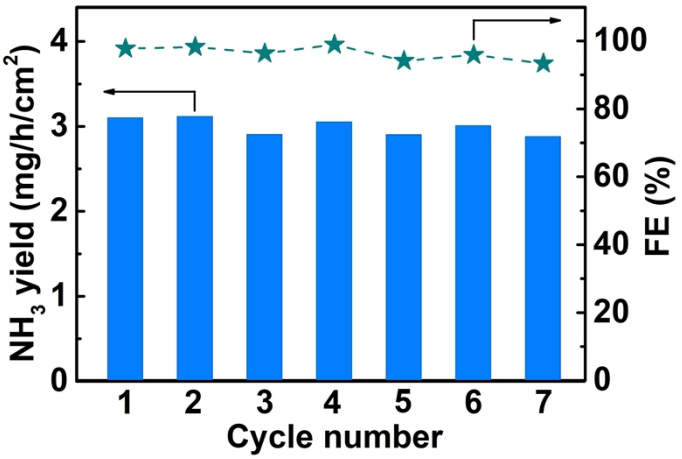

Fig. S7. NH_3 yields and FEs of $NiFe_2O_4$/CC for recycling tests at −0.6 V in 0.1 M PBS with additional 0.1 M $NaNO_3$.

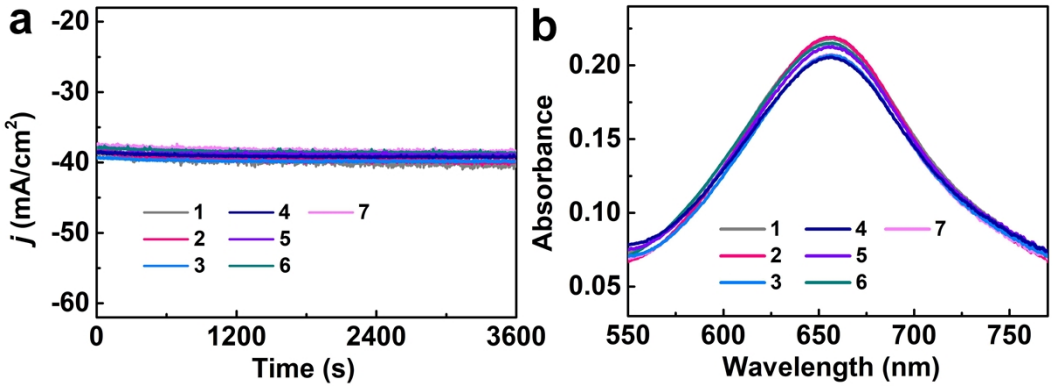

Fig. S8. (a) Chronoamperometry curves and corresponding UV-Vis spectra of $NiFe_2O_4$/CC for generated NH_3 during recycling tests at −0.6 V in 0.1 M PBS with additional 0.1 M $NaNO_3$.

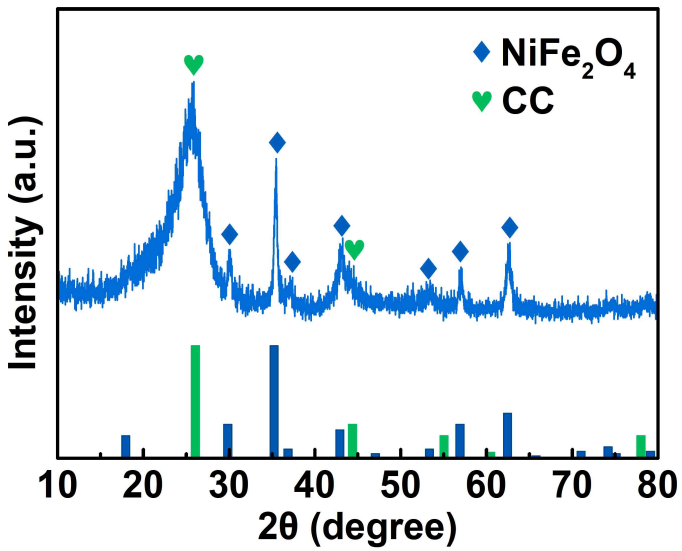

Fig. S9. XRD pattern for $NiFe_2O_4$/CC after electrolysis test.

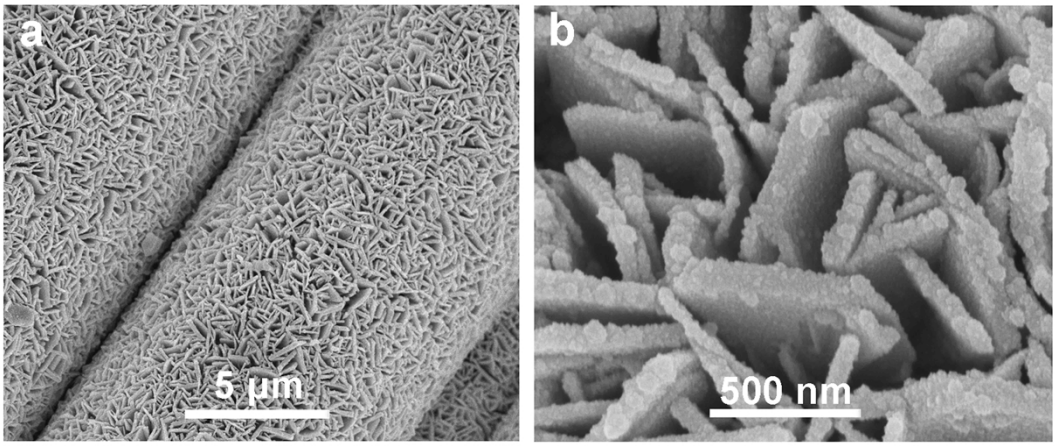

Fig. S10. SEM images for $NiFe_2O_4$/CC after electrolysis test.

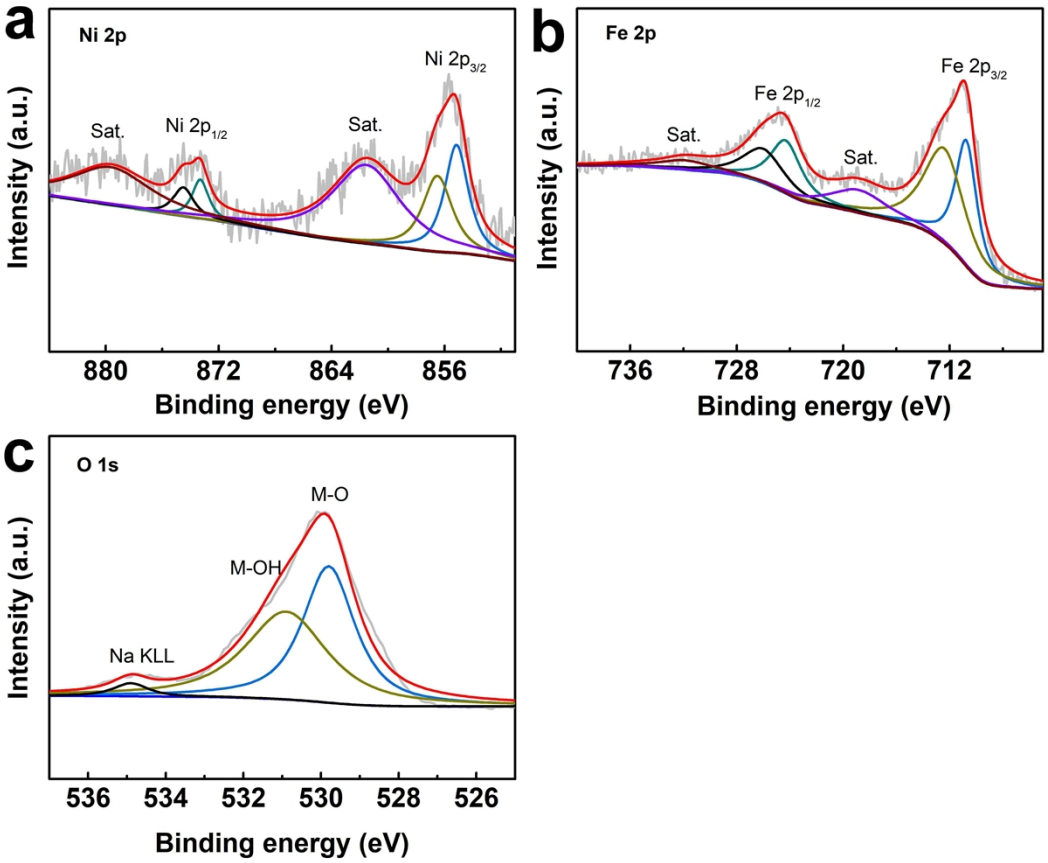

Fig. S11. XPS spectra in (a) Ni 2p, (b) Fe 2p, and (c) O 1s regions for $NiFe_2O_4$/CC after electrolysis test. The peak at 534.9 eV in O 1s region can be assigned to the Na KLL Auger line which is derived from the electrolyte adsorbed on the surface of $NiFe_2O_4$.

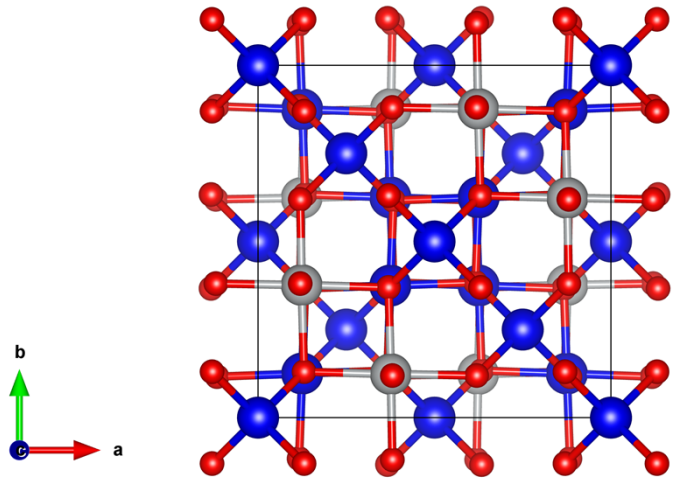

Fig. S12. The atomic structure of $NiFe_2O_4$ with inverse spinel structure.

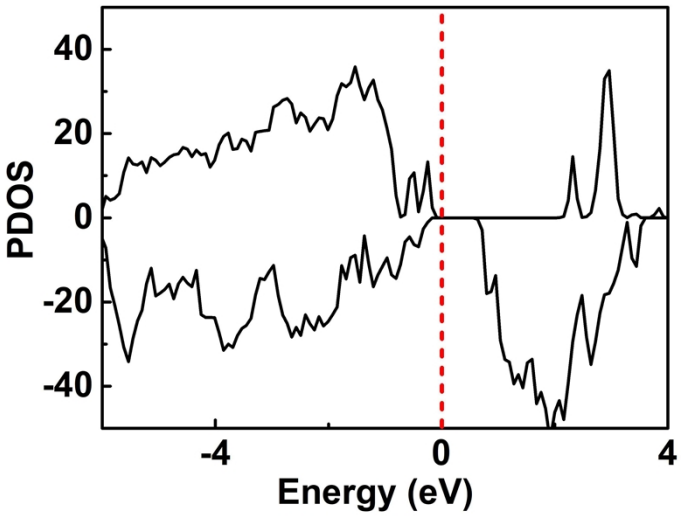

Fig. S13. PDOS of $NiFe_2O_4$ bulk.

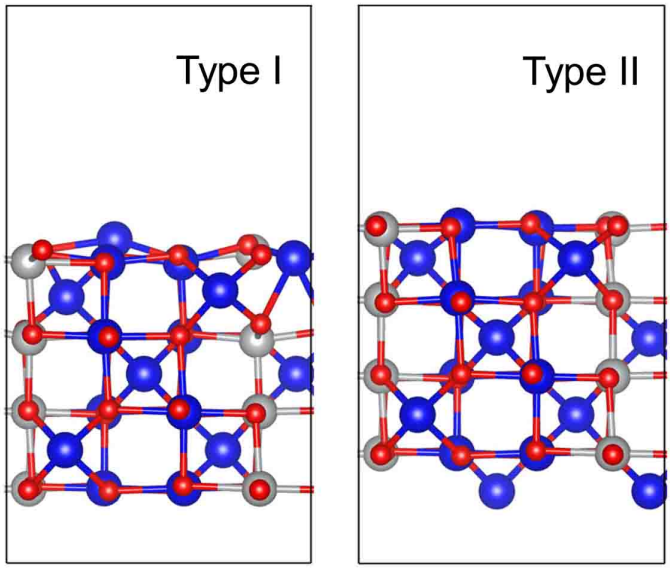

Fig. S14. $NiFe_2O_4$ (100) surface with two terminations.

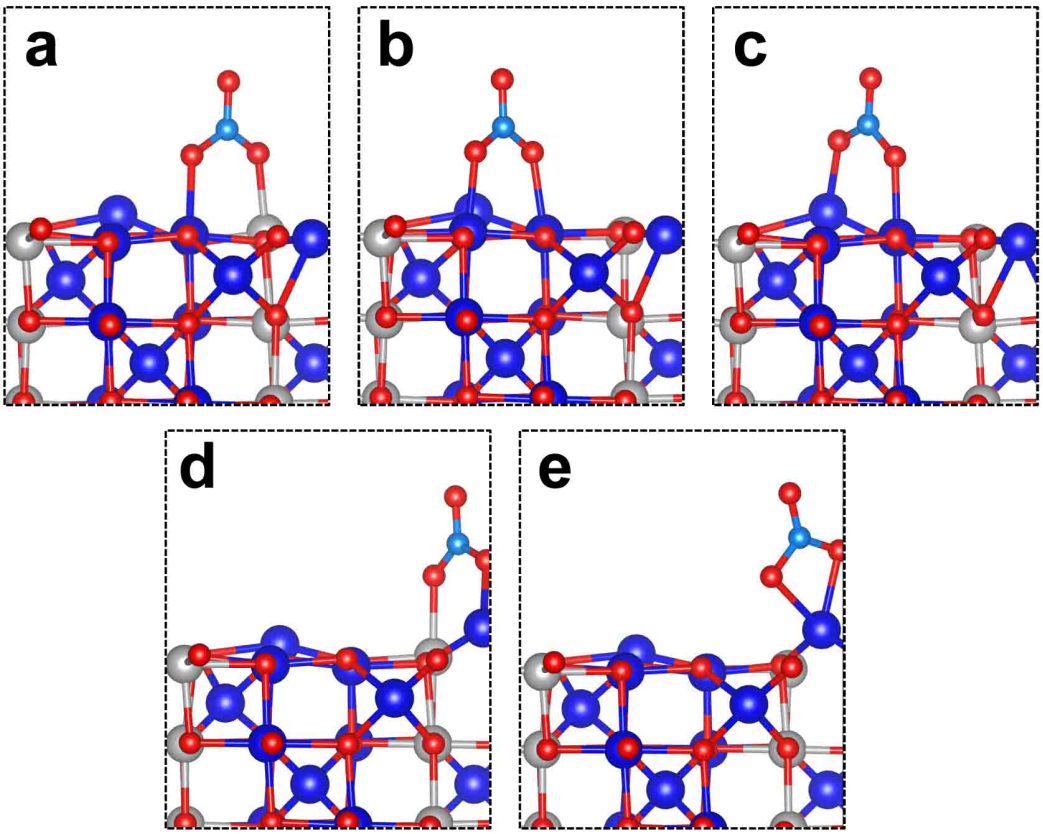

Fig. S15. The NO_3^- adsorption configurations on $NiFe_2O_4$ (100) surface.

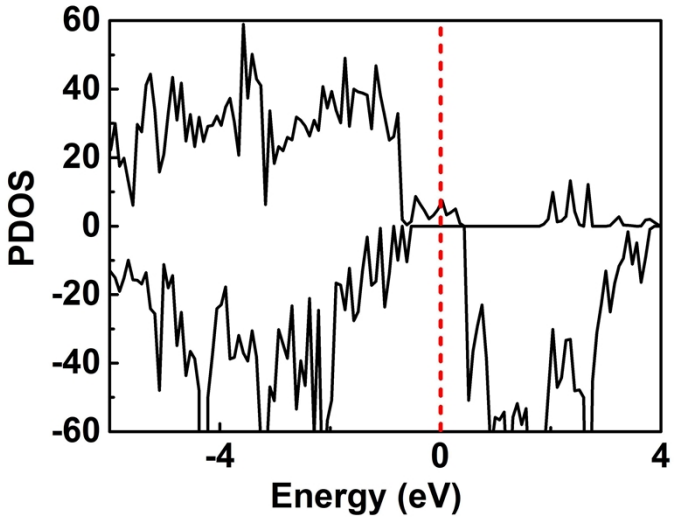

Fig. S16. PDOS of $NiFe_2O_4$ (100).

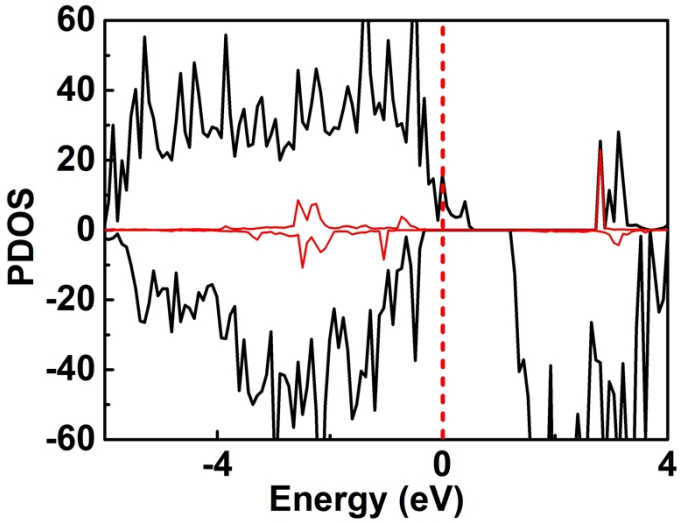

Fig. S17. PDOS of NO_3^- adsorbed on $NiFe_2O_4$ (100).

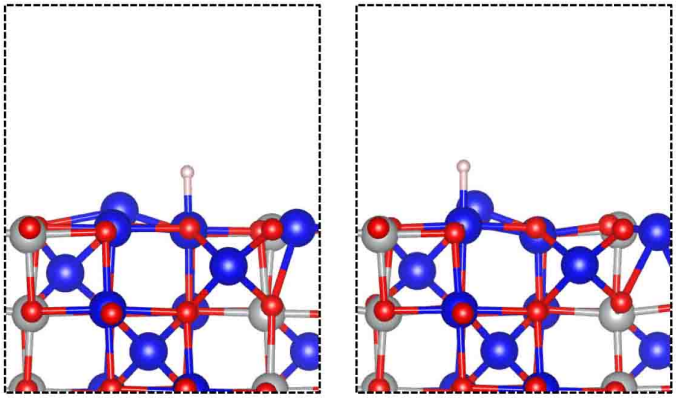

Fig. S18. Atomic configurations of H adsorbed on different site of $NiFe_2O_4$ (100).

Table S1. Comparison of the FE and NH_3 yield for $NiFe_2O_4$/CC with other reported non-noble-metal eNO_3RR catalysts.

Catalyst	Electrolyte	FE (%) @ E (V vs RHE)	NH_3 yield ($mg/h/cm^2$) @ E (V vs RHE)	Ref.
$NiFe_2O_4$/CC	**0.1 M PBS (0.1 M $NaNO_3$)**	**96.6 @ –0.60**	**10.6 @ –1.0**	**This work**
Fe SAC	0.1 M K_2SO_4 (0.5 M KNO_3)	75.0 @ –0.66	8.0 @ –0.85	8
Fe-PPy SACs	0.1 M KOH (0.1 M KNO_3)	100 @ −0.50	2.75 @ −0.70	9
O-Cu-PTCDA	0.1 M PBS (4.95 mM KNO_3)	85.9 @ −0.4	0.90 @ −0.6	10
Cu_3P NA/CF	0.1 M PBS (0.1 M $NaNO_3$)	62.9 @ −0.60	0.848 @ −0.9	11
Cu/Cu_2O NWAs	0.5 M Na_2SO_4 (2.36 mM $NaNO_3$)	95.8 @ −0.85	4.1633 @ −0.85	12
pCuO-5	0.05 M H_2SO_4 (0.05 M $NaNO_3$)	89.0 @ −0.5	4.964 @ −0.6	13
In-S-G	0.1 M KOH (0.1 M KNO_3)	75.0 @ −0.5	1.272 @ −0.5	14
oxo-MoS_x	0.1 M PBS (0.1 M $NaNO_3$)	96.0 @ 0	—	15
TiO_{2-x}	0.5 M Na_2SO_4 (0.59 mM $NaNO_3$)	85.0 @ −0.95	0.765 @ −0.95	16
Ni_3N/N-C-800	0.5 M Na_2SO_4 (0.05 M $NaNO_3$)	85.0 @ −0.795	4.72 @ −0.795	17
BCN@Ni	0.1 M KOH (0.1 M KNO_3)	90.0 @ −0.3	2.25 @ −0.5	18
Ni_3B@$NiB_{2.74}$	0.1 M KOH (0.1 M KNO_3)	100.0 @ −0.3	0.012 @ −0.3	19
Co_3O_4@NiO	0.5 M Na_2SO_4 (2.36 mM $NaNO_3$)	55.0 @ −0.7	—	20

References

1 G. Kresse and J. Hafner, Ab initio molecular-dynamics simulation of the liquid-metal-amorphous-semiconductor transition in germanium, *Phys. Rev. B*, 1994, **49**, 14251–14269.

2 G. Kresse and D. Joubert, From ultrasoft pseudopotentials to the projector augmented-wave method, *Phys. Rev. B*, 1999, **59**, 1758–1775.

3 J. P. Perdew, K. Burke and M. Ernzerhof, Generalized gradient approximation made simple, *Phys. Rev. Lett.*, 1996, **77**, 3865–3868.

4 F. Liu, J. Liu, R. Fang, Y. Li and Y. Yang, Different reactivities of the (100) and (110) surfaces of the $NiFe_2O_4$ composite oxygen carrier in chemical looping combustion: an atomic insight, *J. Phys. Chem. C*, 2021, **125**, 19190–19199.

5 X. Shi, S. L. Bernasek and A. Selloni, Mechanism and activity of CO oxidation on (001) and (110) surfaces of spinel Co_3O_4, $NiCo_2O_4$ and $NiFe_2O_4$: a DFT + U study, *Surf. Sci.*, 2018, **677**, 278–283.

6 H. J. Monkhorst and J. D. Pack, Special points for Brillouin-zone integrations, *Phys. Rev. B*, 1976, **13**, 5188–5192.

7 V. Wang, N. Xu, J.-C. Liu, G. Tang and W.-T. Geng, VASPKIT: a user-friendly interface facilitating high-throughput computing and analysis using VASP code, *Comput. Phys. Commun.*, 2021, **267**, 108033.

8 Z.-Y. Wu, M. Karamad, X. Yong, Q. Huang, D. A. Cullen, P. Zhu, C. Xia, Q. Xiao, M. Shakouri, F.-Y. Chen, J. Y. Kim, Y. Xia, K. Heck, Y. Hu, M. S. Wong,

Q. Li, I. Gates, S. Siahrostami and H. Wang, Electrochemical ammonia synthesis via nitrate reduction on Fe single atom catalyst, *Nat. Commun.*, 2021, **12**, 2870.

9 P. Li, Z. Jin, Z. Fang and G. Yu, A single-site iron catalyst with preoccupied active centers that achieves selective ammonia electrosynthesis from nitrate, *Energy Environ. Sci.*, 2021, **14**, 3522–3531.

10 G.-F. Chen, Y. Yuan, H. Jiang, S.-Y. Ren, L.-X. Ding, L. Ma, T. Wu, J. Lu and H. Wang, Electrochemical reduction of nitrate to ammonia via direct eight-electron transfer using a copper-molecular solid catalyst, *Nat. Energy*, 2020, **5**, 605–613.

11 J. Liang, B. Deng, Q. Liu, G. Wen, Q. Liu, T. Li, Y. Luo, A. A. Alshehri, K. A. Alzahrani, D. Ma and X. Sun, High-efficiency electrochemical nitrite reduction to ammonium using a Cu_3P nanowire array under ambient conditions, *Green Chem.*, 2021, **23**, 5487–5493.

12 Y. Wang, W. Zhou, R. Jia, Y. Yu and B. Zhang, Unveiling the activity origin of a copper-based electrocatalyst for selective nitrate reduction to ammonia, *Angew. Chem. Int. Ed.*, 2020, **59**, 5350–5354.

13 R. Daiyan, T. Tran-Phu, P. Kumar, K. Iputera, Z. Tong, J. Leverett, M. H. A. Khan, A. Asghar Esmailpour, A. Jalili, M. Lim, A. Tricoli, R.-S. Liu, X. Lu, E. Lovell and R. Amal, Nitrate reduction to ammonium: from CuO defect engineering to waste NO_x-to-NH_3 economic feasibility, *Energy Environ. Sci.*, 2021, **14**, 3588–3598.

14 F. Lei, W. Xu, J. Yu, K. Li, J. Xie, P. Hao, G. Cui and B. Tang, Electrochemical synthesis of ammonia by nitrate reduction on indium incorporated in sulfur doped graphene, *Chem. Eng. J.*, 2021, **426**, 131317.

15 Y. Li, Y. K. Go, H. Ooka, D. He, F. Jin, S. H. Kim and R. Nakamura, Enzyme mimetic active intermediates for nitrate reduction in neutral aqueous media, *Angew. Chem. Int. Ed.*, 2020, **59**, 9744–9750.

16 R. Jia, Y. Wang, C. Wang, Y. Ling, Y. Yu and B. Zhang, Boosting selective nitrate electroreduction to ammonium by constructing oxygen vacancies in TiO_2, *ACS Catal.*, 2020, **10**, 3533–3540.

17 X. Zhang, G. Ma, L. Shui, G. Zhou and X. Wang, Ni_3N nanoparticles on porous nitrogen-doped carbon nanorods for nitrate electroreduction, *Chem. Eng. J.*, 2022, **430**, 132666.

18 X. Zhao, Z. Zhu, Y. He, H. Zhang, X. Zhou, W. Hu, M. Li, S. Zhang, Y. Dong, X. Hu, A. V. Kuklin, G. V. Baryshnikov, H. Ågren, T. Wågberg and G. Hu, Simultaneous anchoring of Ni nanoparticles and single-atom Ni on BCN matrix promotes efficient conversion of nitrate in water into high-value-added ammonia, *Chem. Eng. J.*, 2022, **433**, 133190.

19 L. Li, C. Tang, X. Cui, Y. Zheng, X. Wang, H. Xu, S. Zhang, T. Shao, K. Davey and S.-Z. Qiao, Efficient nitrogen fixation to ammonia through integration of plasma oxidation with electrocatalytic reduction, *Angew. Chem. Int. Ed.*, 2021, **60**, 14131–14137.

20 Y. Wang, C. Liu, B. Zhang and Y. Yu, Self-template synthesis of hierarchically structured Co_3O_4@NiO bifunctional electrodes for selective nitrate reduction and tetrahydroisoquinolines semi-dehydrogenation, *Sci. China Mater.*, 2020, **63**, 2530–2538.